Received: 29 June 2022 | Revised: 6 December 2022 | Accepted: 29 December 2022

DOI: 10.1111/jace.18985

Journal of the American Ceramic Society

RESEARCH ARTICLE

Effects of sintering and zirconmullite doping on nanostructural vacancies of bovine hydroxyapatite by positron techniques

Leyla Nur Akay[1] | **Cevriye Kalkandelen**[2] | **Necmettin Akti**[1] | **Merve Sazimet Sengul**[1] | **Cumali Tav**[1] | **Ugur Yahsi**[1] | **Ziya Engin Erkmen**[3]

[1]Department of Physics, Faculty of Science, Marmara University, Kadikoy, Istanbul, Turkey

[2]Department of Biomedical Devices Technology, Vocational School of Technical Sciences, Istanbul University-Cerrahpasa, Istanbul, Turkey

[3]Metallurgical and Materials Engineering Department, Faculty of Engineering, Marmara University, Maltepe, Istanbul, Turkey

Correspondence
Ugur Yahsi, Department of Physics, Faculty of Science, Marmara University, Istanbul, Turkey.
Email: uyahsi@marmara.edu.tr

Ziya Engin Erkmen, Metallurgical and Materials Engineering Department, Faculty of Engineering, Marmara University, Istanbul, Turkey.
Email: zeerkmen@gmail.com

Funding information
Marmara Üniversitesi, Scientific Research Projects Committee, Grant/Award Number: FEN-A-200716-0376

Abstract

In this study, the nanostructural vacancy behavior of bovine derived hydroxyapatite (BHA) doped with powder zirconmullite (ZM) contents of 5, 7.5, 10 and 12.5 wt.% were presented at sintering temperatures of 1000, 1100, 1200 and 1300°C. ZM-doped BHA (ZM-BHA) was characterized by X-ray diffraction and positron annihilation lifetime spectroscopy (PALS). Density and hardness behavior were measured with respect to increasing sintering temperature. PALS results indicate that the longest lifetime component τ_3 of ortho-positronium (o-Ps) localized at open spaces is attributed to the vacancy site and almost constant with the ZM contents and the sintering temperatures to have a mean value of 0.680 ns (corresponding to the radius of 0.997 nm). This average value is ascribed to the OH group defects along the main crystalline line. On the other hand, the o-Ps intensity attributed to the number of vacancy sites increases almost linearly with ZM additives and sintering temperatures. The intensity is also related to the density and hardness of ZM-BHA in terms of ZM contents.

KEYWORDS
bovine hydroxyapatite, mechanical properties, positron annihilation lifetime spectroscopy (PALS), vacancy, zirconmullite

1 | INTRODUCTION

Calcium phosphate ceramics are widely used in medicine due to their high biocompatibility and ability to grow bone around the implant material. The single, biphasic, triphasic and multiphasing single component calcium phosphate and ortophosphate ceramics are extensively studied and their biomedical applications and coatings are reviewed and summarized in the references.[1-4] The load bearing capacity of these bioceramics is usually increased with the addition of inert oxides such as zirconia, titania, magnezia, etc. and their use in ortopaedics and dentistry are studied.[5-10] The mechanical properties of zirconia ceramics alone coated with calcium deficient hydroxyapatite (HA) was also investigated in a more recent research.[11] The effect of oxide additions on the crystal structure vis-a-vis atom coordinates of HA is not fully understood, and they form regular composite mixtures. The solid solutions of oxide addition, if any, with the matrix and the corresponding biological behavior of cell tissues against the modified crystal

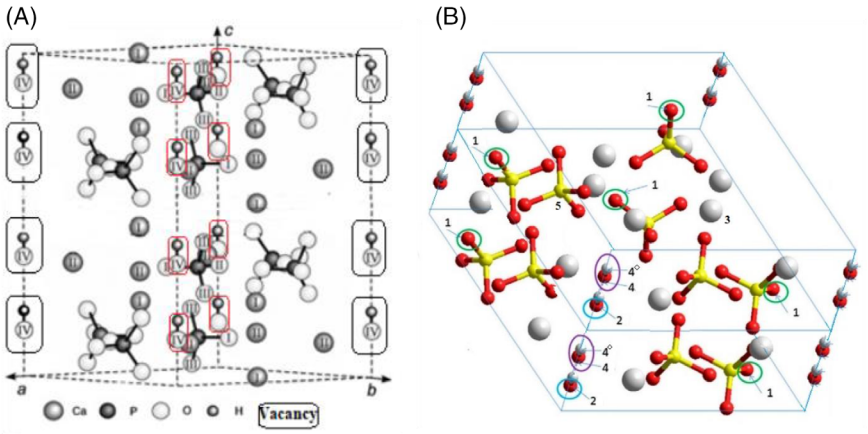

FIGURE 1 The molecular configuration of an hexagonal HA cell containing 88 atoms adopted from 1 and 23 showing probable OH vacancy channels along *c* axis in (A) 2D and (B) 3D (circle 1 indicates single oxygen atom vacancy probable in PO_4 groups, circle 2 indicates probable O vacancy in the OH channel, circle 3 indicates Calcium atom, circles 4 and 4^+ indicate OH vacancy, and circle 5 indicates Phosphorous atom).

should be investigated. Bovine-derived HA (BHA) is one of the most preferred natural HA types.[4,10-12] BHA is usually produced using diluted HCI acid, which enables demineralization and freeze-drying of the tissues. Even when strict regulations are applied, some deadly high-priority diseases (bovine spongiform encephalopathy) can survive even after all controlled processes. High temperature calcination performed at 850°C, prevents these diseases from occurring.

Defects in these HA structures promote better biocompatibility, adhesion, attachment of bone cells, and proliferation than those in biological structures. For this reason, we concentrate the defect vacancy analysis of ZM-BHA materials. A very comprehensive study on defect modeling of pure HA was performed by Bystrow et al.[13] and Matsunaga et al.[14] who modeled defects and electronic structures in their work: they pretended the formation of V_O^-,V_H^+, V_{OH}^-, and V_{Ca}^{++} vacancies in HA, because these vacancies were expected to be relatively easy to form HA energetically with increasing temperature 1073 K in a simple hexagonal structure. The common structural defects of Ca and OH ions in HA are located along the main structural *c* axis so called 'OH-channel'. Especially OH-OH vacancies form along the *c* axis, in a hexagonal supercell of 88 atoms leading to the non stochiometric HA and its derivatives in ambiant atmosphere with water vapor at low pressure following the postulated reaction[15,16] as in Figure 1:

$$Ca_{10}(PO_4)_6(OH)_2 \rightarrow Ca_{10}(PO_4)_6(OH)_{2-2x}O_x(V_{OH})_x + xH_2O_{gas} \quad (1)$$

To understand further the bone tissue structure with vacancy defects, one of the relatively less-known methods such as measurement of the free volume of the bone tissue, can be used. Free volume as a measure of the vacancy exists in the tissues as the chemical structure changes by the substitutional components and the sintering temperatures. Actually, the free volume quantity can be correlated with some physical phenomena, such as the glass transition temperature,[17] viscosity,[18-21] ionic conductivity,[22] relaxation[23] and other mechanical and thermodynamic properties. Some methods, such as differential scanning calorimetry (DSC), X-ray diffraction (XRD), dynamic mechanical analysis (DMA), FTIR, electron microscopy, and neutron scattering, are used to estimate the free volume indirectly.[17] However, as a powerful nondestructive technique, positron annihilation lifetime spectroscopy (PALS) provides invaluable information about the structure of materials.[17] PALS is a unique technique to measure the size, density and size distribution of the free volume in materials.[17] Zirconmullite (ZM) is an inert material very stable at temperatures over 1000°C and is composed of zirconia (ZrO_2) and mullite ($3Al_2O_3.2SiO_2$) as a mechanical mixture of both phases simultaneously. The structural and physical properties of BHA with/without ZM may be important in terms of its usage in medicine, nanotechnology and photocatalytic processes. On the other hand, defects in BHA play an important role in their usage. Defect analysis of BHA with/without ZM has not been studied very well. Especially during the sintering and substitution of ZM, some vacancy defects, such as OH, Ca and O vacancies, can be produced that might be important in the usage of ZM-BHA.

In this study, the physical and mechanical properties of ZM-doped BHA composites were investigated in terms of changes in microscopic free volume using PALS.

2 | MATERIALS AND METHODS

2.1 | Raw materials

Zirconmullite powder was obtained from Haznedar Durer Company with a weight averaged particle size of 1.524 mm and density 1.69 g/cm^3. Its chemical analysis is provided in Table 1.

TABLE 1 Chemical analysis of zircon mullite powder in wt%

Al_2O_3	ZrO_2	SiO_2	Na_2O	Fe_2O_3	CaO	TiO_2
46.47	35.31	17.87	0.09	0.07	0.04	0.15

Alumina versus Silica molecular ratio (46.47/102):(17.87/60) = 1.53 confirms the presence of mullite, which is also proved by XRD analysis and mullite versus zirconia weight ratio is found to be 1.82. Hydroxyapatite produced from calf femur bone by boiling following calcining in a muffle furnace were used.

2.2 | Preparation of bovine hydroxyapatite composite strengthened with zirconmullite

Fresh bovine femoral bone was obtained from a butcher and boiled for nearly 2 h to be released from its soft tissues. Then, it was calcinated in a box furnace at 850°C for 4 h under ambient atmosphere. Calcinated bovine has obtained a completely white color free of its organic substances. Crushing and milling using a mortar grinder and planetary ball mill was used to obtain the powder, which was dry sieved to under 75 μm. The sieved powder was mixed with zirconmullite at 5, 7.5, 10, and 12.5 wt% using ball milling for 4 h with alumina media. Powder mixtures were pressed in hardened steel molds according to British Standard 7253 with a one-way press at 350 MPa pressure. The resulting pellets are 11 mm in diameter and 11 mm in height. The composite pellets were then sintered at 1000, 1100, 1200 and 1300°C for 4 h in ambient atmosphere.

2.3 | PALS

In working PALS, a setup of a fast-fast coincidence system was used, based on the measurement of the time interval between the birth signal as 1274 keV prompt gamma and the stop signal as 511 keV positron annihilation gamma. To detect both γ rays, two plastic scintillators (BC422) with photomultiplier tubes (PMT) (Hamamatsu R2059) and ORTEC Base, and for the timing signals and timing, two constant fractional differential discriminators (ORTEC 583B) and a time-to-amplitude converter (ORTEC 266) connected to the MCA time spectrum (ORTEC ASPEC 927) were used. To extract the lifetimes and their intensities in the time spectrum, the LT9.2 code program[24] was applied. This LT code is a respected analysis program to fit PALS data that are deconvoluted of the lifetime spectrum into a number of exponential components.

The PALS spectrum in three lifetime components was also analyzed: of bound state positronium, one is the singlet state of the antiparallel spins so-called para-positronium (p-Ps) with the corresponding lifetime (τ_1) with its intensity (I_1) and the other is the triplet state of antiparallel spins so-called ortho-positronium (o-Ps) with the corresponding lifetime (τ_3) with its intensity (I_3), and free positron has a contribution as a direct annihilation lifetime (τ_2) with the intensity (I_2). A relation can be established between the lifetime and geometric structure of the cavity where o-Ps resides, using the overlap integration of the Ps wave function. For this purpose, the Tao–Eldrup model[25,26] was used. In this model, o-Ps was considered to be in a spherical potential well of radius R with a surrounding electron cloud layer of thickness $\delta R = R_0 - R$. The model in the ground state of the Ps wave function reads as

$$\frac{1}{\tau_3(ns)} = 2\left(1 - \frac{R}{R_0} + \frac{1}{2\pi}\sin\frac{2\pi R}{R_0}\right) \quad (1)$$

where $\delta R = 0.1656$ nm is empirically determined value.[17,27] The hole-free volume (υ_f) then follows as:

$$\upsilon_f(\tau_3) = 4\pi R^3/3 \quad (2)$$

3 | RESULTS AND DISCUSSION

3.1 | XRD results

X-ray diffraction phase analysis (XRD) of pure zircon mullite and composite samples (12.5 wt.%) sintered at 1000, 1100, 1200 and 1300°C was performed with a Bruker d2 phaser instrument using CuKα radiation (λ = 1.541 Å) with 30 kV, 10 A conditions, and the results are shown in Figure 2. In Figure 2, two main phases were determined: the first is mullite (PDF 74–4144) with the chemical formula $Al_{4.52}Si_{1.48}O_{9.74}$ with an orthorhombic crystal structure[15,16] and the second phase is badeleyite (PDF 37–1484) with the chemical formula ZrO_2 with a monoclinic crystal structure. The peaks in the graph are compatible with the literature.[4,10,15,28-30]

When sintered from 1000 to 1300°C, the pure synthetic BHA changed color from white to blue, especially after 1200°C, which was possibly due to phase transformations and related to variations in electron transitions in the d orbitals of newly formed phases. In Figure 3, when 12.5 wt.% ZM was added to BHA, after the 1100°C heat treatment, the initial BHA phases were stable, as no change occurred in the diffraction pattern (PDF: 01-075-3726). However after 1200°C heat treatment, the amount of BHA decreased as can be noticed from peak magnitudes whereas some new phase whitlockite formed

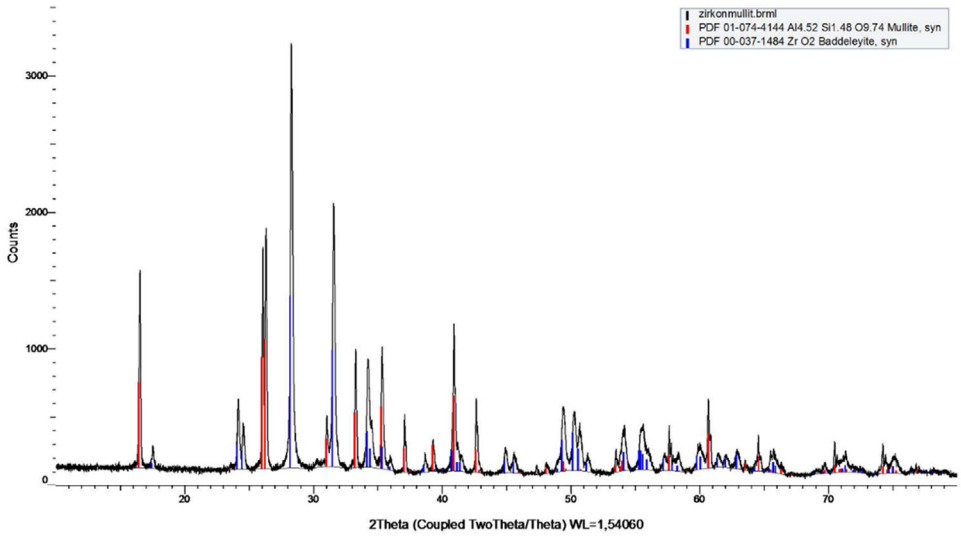

FIGURE 2 X-ray diffraction (XRD) results of pure zirconmullite

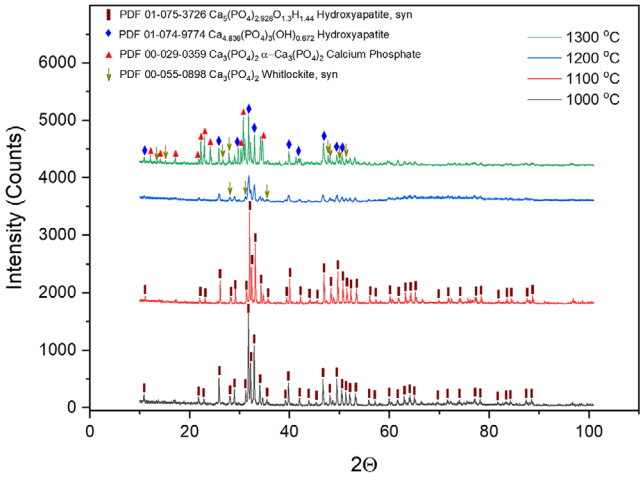

FIGURE 3 X-ray diffraction (XRD) results of bovine derived hydroxyapatite (BHA) mixed with 12.5 wt.% zirconmullite (ZM) sintered at 1000–1300°C

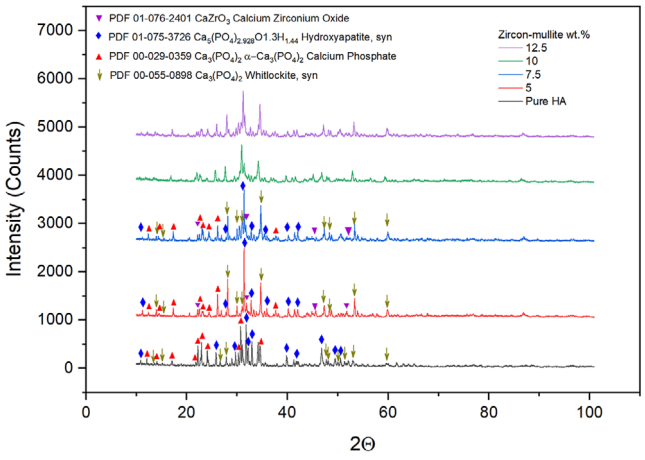

FIGURE 4 X-ray diffraction (XRD) results of pure and alloyed bovine derived hydroxyapatite (BHA) with zirconmullites (ZMs) of 5, 7.5, 10, and 12.5 wt.% followed by heat treatment at 1300°C

(PDF: 00-055-0898). After 1300°C heat treatment, BHA transformed to Ca deficient HA and Ca^{++} ions content dropped from 5 to 4.36 (PDF: 01-074-9774) and in contrast, $(PO_4)^{-IV}$ stoichiometry increased from 2.928 to 3 and the OH^- hydroxyle stochiometry dropped from nearly 1.3 to 0.672 possibly forming OH channels and H vacancies. Additionally, the unit hexagonal cell volume increased from $V = 528.83$ Å^3 to 529.12 Å^3, indicating new formation of vacant spaces in the lattice following whitlockite. After 1300°C heat treatment, the calcium phosphate phase (PDF: 00-029-0359) and minor amount of calcium zirconium oxide also appeared at the expense of original BHA which transformed to Ca-deficient hydroxyapatite (PDF: 01-074-9774). Figure 4 is the representation of heat-treated BHA with 5, 7.5, 10, and 12.5 wt.% ZM additions sintered at 1300°C. Pure BHA sintered at 1300°C is provided as the control diffractogram for alloyed samples. As can be observed, in addition to whitlockite, hydroxyapatite, and calcium phosphate phases, as determined previously, the calcium zirconium oxide phase (PDF: 01-076-2401) formed additionally as a result of alloying and heat treatment. When comparing the patterns with each other in Figure 4, it can be concluded that there is a slight decrease in calcium phosphate content following the addition of ZM, possibly enhancing the formation of the calcium zirconium oxide phase.

The greater the complexity of the pattern increases, the most likely the formation intercavities and atomic size vacancies and defects in the composite. The results are compatible with the literature.[31-33]

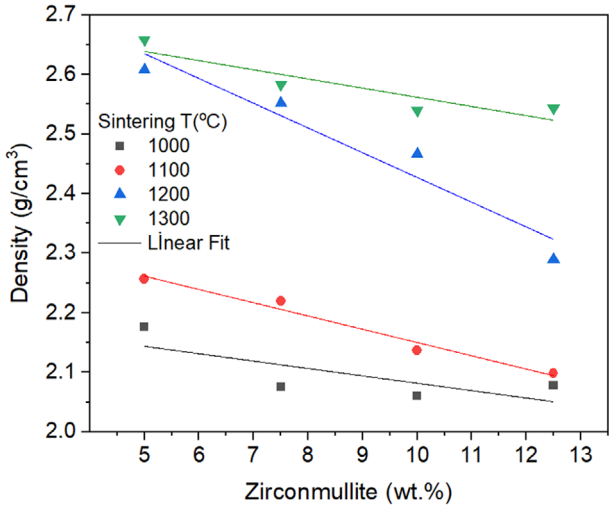

FIGURE 5 Density of bovine derived hydroxyapatite (BHA) with respect to zirconmullite (ZM) addition at different sintering temperatures. The best fit line is drawn for each data set

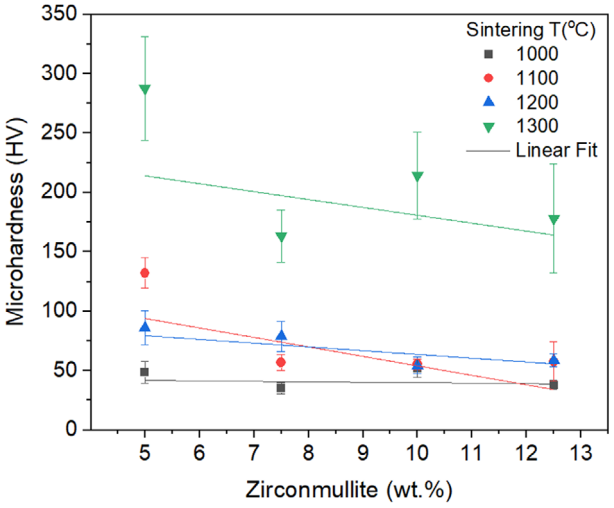

FIGURE 6 Hardness of bovine derived hydroxyapatite (BHA) with respect to zirconmullite (ZM) (wt.%) at sintering temperatures. The best fit line is drawn for each data set.

3.2 | Density and hardness of HA with zirconmullite

The density and hardness results are plotted in Figures 5 and 6, respectively. Density measurements of sintered samples were evaluated using the Archimedes method, and the hardness was measured using a Vickers micro indenter.

As shown in Figure 5, a linear decrease in density occurred with increasing alloy content, and an increase was observed with increasing sintering temperature, as expected. From Figure 6, it is observed that a significant increase in microhardness is apparent at 1300°C due to enhanced diffusion causing higher density and possibly to whitlockite and calcium zirconium oxide phase formations. Increasing alloy content caused a slight decrease in microhardness, although it significantly decreased the density of composites, possibly due to volumetric changes during phase transformations and corresponding thermal expansions of newly formed phases.

3.3 | PALS results of bovine hydroxyapatite with zirconmullit additives

PALS experiments were carried out with two pieces of the samples with more than 2 mm thickness each, sandwiching the positron source approximately 30 μCi of ^{22}NaCl on a thin aluminum foil (5 μm thick). We have a resolution of approximately 350 ps. We have taken a million counts for each sample measurement.

To analyze the PALS spectrum, the p-Ps lifetime value $\tau_1 = 125$ ps in vacuum was selected assuming it stayed constant in matter. PALS lifetimes and their intensities and the defect volume (υ_f) are in Table 2 for BHA-ZM composites for sintering temperatures 1000, 1100, 1200 and 1300°C. The o-Ps lifetime is approximately 0.680 ± 0.03 ns corresponding to 0.0997 nm radius using Equation (1). This value is close to the OH^- ion radius of 0.11 nm and the O^- ion radius of 0.126 nm and the Ca^{++} ion radius of 0.114 nm.[13,14,34]

In Figure 7, the o-Ps intensity is plotted with respect to increasing sintering temperatures for each ZM content (5, 7.5, 10 and 12.5 wt.%). The solid lines are the best-fit regression lines to each ZM content separately. For each ZM content, the o-Ps intensity as a measure of the number of defects increases linearly with the sintering temperature. Increasing the sintering temperature might have caused OH bonds to brake and then evaporate as H_2O vapor, leaving the vacant side behind. These crystal defects also increase linearly with the increase in ZM content due to mismatch with the matrix (BHA), creating new surfaces and increasing the internal energy.

In Figure 8, the o-Ps intensity is replotted with respect to the ZM content for each sintering temperature, and the solid lines are the best-fit regression lines. For each sintering temperature, the o-Ps intensity increases almost linearly with ZM content, except for one datum with 12.5 wt.% at 1300°C, which was reduced drastically, claiming to the partial structural collapse with the increasing defects. The slopes of the best fit lines also increase to 0.375, 0.800, 1.186 and 1.549 for sintering temperatures of 1000, 1100, 1200 and 1300°C, respectively. Although ZM addition increased the defect concentration, which affected the PALS results, it caused a decrease in the density and hardness due to phase transformations at high temperatures over 1100°C.

TABLE 2 Positron annihilation lifetime spectroscopy (PALS) parameters as lifetimes (τ_2 and τ_3) and intensities (I_2 and I_3) with hole radius (R) in terms of temperature for zirconmullite (ZM) contents from 5% to 12.5%

Anneal T(°C)	ZM Content (%)	τ_2 (ns) (± 0.086)	I_2 (%) (± 1.4)	τ_3 (ns) (± 0.03)	I_3 (%) (± 0.47)	R(nm) (± 0.008)
1000°C	0	0.261	80.3	0.710	4.55	0.107
	5	0.265	76.5	0.670	6.22	0.097
	7.5	0.269	78.2	0.710	6.97	0.108
	10	0.268	79.2	0.660	8.87	0.094
	12.5	0.275	74.1	0.680	8.40	0.099
1100°C	0	0.255	79.4	0.670	4.65	0.097
	5	0.266	80.2	0.650	8.61	0.092
	7.5	0.276	78.4	0.660	11.9	0.094
	10	0.285	73.8	0.675	12.1	0.100
	12.5	0.292	72.1	0.675	14.7	0.099
1200°C	0	0.254	70.9	0.678	5.72	0.099
	5	0.288	73.2	0.670	12.3	0.097
	7.5	0.321	64.7	0.724	14.4	0.110
	10	0.313	68.6	0.717	17.4	0.109
	12.5	0.301	66.8	0.670	21.8	0.097
1300°C	0	0.289	58.0	0.650	8.27	0.092
	5	0.312	69.5	0.700	15.2	0.105
	7.5	0.317	67.5	0.697	19.1	0.104
	10	0.294	66.6	0.660	23.8	0.094
	12.5	0.305	68.9	0.675	20.6	0.099

Note: The intensities were normalized as $I_1 + I_2 + I_3 = 1$.

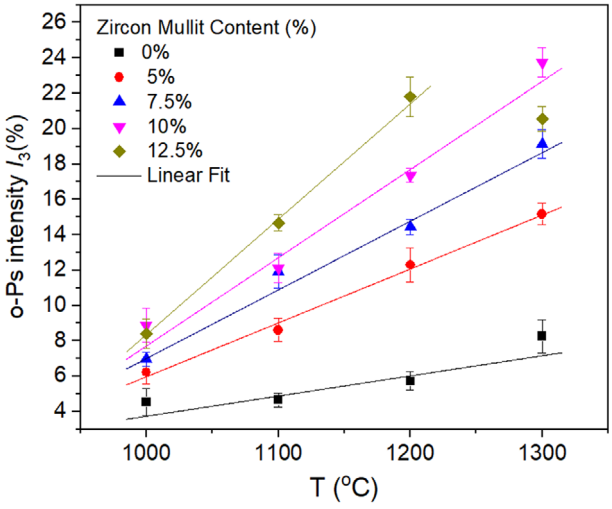

FIGURE 7 The o-Ps lifetime intensity versus sintering temperature with increasing zirconmullite (ZM) content

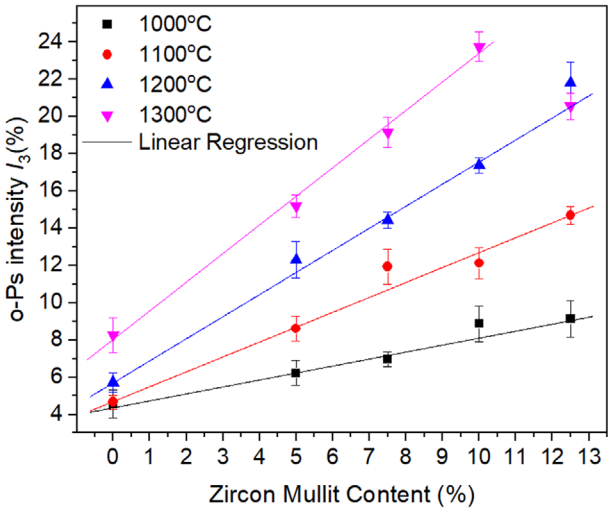

FIGURE 8 The o-Ps lifetime intensity versus the zirconmullite (ZM) content and sintering temperatures

3.4 | SEM analysis

Scanning electron microscope (SEM) analysis was performed using a JEOL 6400 instrument in BSE (Back scattered electron imaging) mode. Figure 9A,B illustrate BHA doped with 12.5 wt.% ZM micrographs taken at 500x and 2500x magnifications, respectively, sintered at 1300°C for 4 h in ambient atmosphere.

As can be observed in Figure 9, the ZM particles (light color phase[4]) are homogeneously distributed throughout the BHA matrix, some of them forming reaction phases such as $CaZrO_3$, and some of them possibly dissolving in the BHA lattice. BHA grains nearly 3 to 5 microns in size

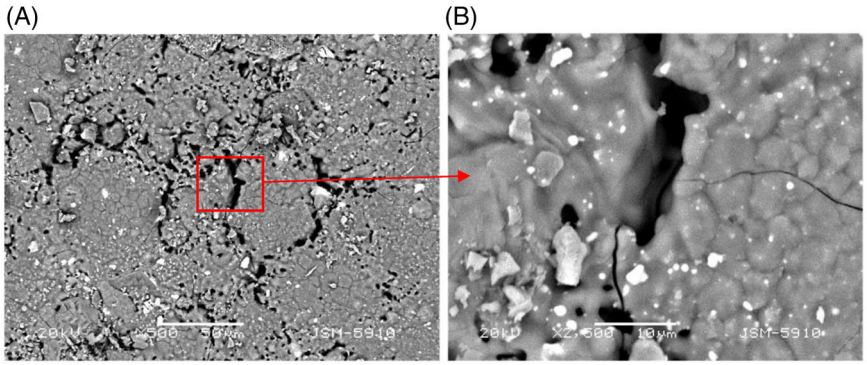

FIGURE 9 SEM micrographs for HA-12.5 zirconmullite (ZM) composite under backscattered electron image (BEI) sintered at 1300°C for 4 h (A) ×500 and (B) ×2500

merge due to high temperature sintering, and wide cracks possibly form during cooling because of the phase contraction and mismatching of various phases with different coefficients of thermal expansion. As the sintering temperature increased, although the density increased with merging grains, micro and nanoporosity increased due to the changing stoichiometry of solid solutions and the generation of new phases causing cracking in the matrix phase.

4 | CONCLUSIONS

The zirconmullite used in this study formed new phases and defects with increasing sintering temperatures. The density and hardness of the composite samples increased as expected with the sintering temperatures, and the phase distributions changed after 1100°C heat treatment, which is consistent with the changes in the o-Ps lifetime intensity. Over 1100°C, the newly formed phases, whitlockite, calcium phosphate and calcium zirconium oxide, affected the molecular structure of the remaining BHA phase, causing defects such as vacant OH and Ca sites, which changed o-Ps lifetime intensity in PALS measurements.

ACKNOWLEDGMENTS

This work has been supported by Marmara Üniversitesi, Scientific Research Projects Committee under Grant (FEN-A-200716-0376). The authors are grateful to research assistants Alaaddin Cem Ok and Şükrü Kaya for performing XRD and heat treatment experiments.

ORCID

Ugur Yahsi https://orcid.org/0000-0002-6587-883X

REFERENCES

1. Dorozhkin SV. Calcium orthophosphate deposits: Preparation, properties and biomedical applications. Materials Science and Engineering: C. 2015, 55:272–326. https://doi.org/10.1016/j.msec.2015.05.033
2. Dorozhkin SV. Multiphasic calcium orthophosphate (CaPO4) bioceramics and their biomedical applications. Ceramics International. 2016, 42(6):6529–54. https://doi.org/10.1016/j.ceramint.2016.01.062
3. Ramesh Bhat GM, Harish P, Vaidya K, Nandakishore B. Zirconia ceramics as a dental biomaterial – an over view. Trends in Biomaterials and Artificial Organs. 2012, 26(3):154–60.
4. Erkmen ZE; Genç Y; Oktar FN. Microstructural and mechanical properties of hydroxyapatite? Zirconia composites. Journal of the American Ceramic Society. 2007, 90(9):2885–92. https://doi.org/10.1111/j.1551-2916.2007.01849.x
5. Bandyopadhyay A; Bernard S; Xue W; Bose S. Calcium phosphate-based resorbable ceramics: influence of MgO, ZnO, and SiO2 dopants. Journal of the American Ceramic Society. 2006;89(9):2675–88. https://doi.org/10.1111/j.1551-2916.2006.01207.x
6. Cetiner BN; Erkmen EZ. Production and characterization of bioglass®-titania reinforced hydroxylapatite composite. Key Engineering Materials. 2011;493–494:566–71. https://doi.org/10.4028/www.scientific.net/KEM.493-494.566
7. Dapporto M; Tampieri A; Sprio S. Composite calcium phosphate/titania scaffolds in bone tissue engineering. Application of titanium dioxide. London, UK: InTech Open; 2017.
8. Kobayashi S; Yamaji S. Prediction of stress-strain curves for TCP/PLLA composites: effect of hydrolysis and strain rate. Advanced Composite Materials. 2015;24(sup1):125–36. https://doi.org/10.1080/09243046.2014.957374
9. Oktar FN; Agathopoulos S; Ozyegin LS; Gunduz O; Demirkol N; Bozkurt Y, et al. Mechanical properties of bovine hydroxyapatite (BHA) composites doped with SiO2, MgO, Al2O3, and ZrO2. Journal of Materials Science: Materials in Medicine. 2007;18(11):2137–43. https://doi.org/10.1007/s10856-007-3200-9
10. Yetmez M; Erkmen ZE; Kalkandelen C; Ficai A; Oktar FN. Sintering effects of mullite-doping on mechanical properties of bovine hydroxyapatite. Materials Science and Engineering: C. 2017, 77:470–5. https://doi.org/10.1016/j.msec.2017.03.290
11. Macan J; Sikirić MD; Deluca M; Bermejo R; Baudin C; Plodinec M, et al. Mechanical properties of zirconia ceramics biomimetically coated with calcium deficient hydroxyapatite. Journal of the Mechanical Behavior of Biomedical Materials. 2020, 111. https://doi.org/10.1016/j.jmbbm.2020.104006
12. Sengor M. Microstructure and mechanical properties of composites of bovine derived hydroxyapatite (BHA) reinforced with MgF2. International Journal of Advances in Engineering and Pure Sciences. 2020, https://doi.org/10.7240/jeps.771433

13. Bystrov V; Paramonova E; Avakyan L; Coutinho J; Bulina N. Simulation and computer study of structures and physical properties of hydroxyapatite with various defects. Nanomaterials. 2021, 11(10). https://doi.org/10.3390/nano11102752
14. Matsunaga K; Kuwabara A. First-principles study of vacancy formation in hydroxyapatite. Physical Review B. 2007, 75(1). https://doi.org/10.1103/PhysRevB.75.014102
15. Aydın H; Gören R. Effect of ulexite on thermal and mineralogical properties of mullite-zirconia composite. Journal of the Australian Ceramic Society. 2017, 53(2):283–6. https://doi.org/10.1007/s41779-017-0034-x
16. Hurwitz FI; Palczer AR; Rogers RB; Peysakhov F; White SP. Development of aluminosilicate aerogel impregnated oxide foams for structurally integrated thermal protection systems. In 36th Annual Conference on Composites, Materials and Structures; January 23–26, 2012; Cape Canaveral, FL.
17. Jean YC, Mallon PE, Schrader DM. Principles and applications of positron & positronium chemistry. Singapore: Word Scientific; 2003.
18. Akdeniz G; Yahsi U; Tav C. Viscous behavior of PS, PP, and ABS in terms of temperature and pressure-dependent hole fraction. Journal of Applied Polymer Science. 2010;117(1):110–3. https://doi.org/10.1002/app.31565
19. Dinc FS; Sedlacek T; Tav C; Yahsi U. On the non-newtonian viscous behavior of polymer melts in terms of temperature and pressure-dependent hole fraction. Journal of Applied Polymer Science. 2014;131(15):n/a. https://doi.org/10.1002/app.40540
20. Sahin-Dinc F; Sorrentino A; Tav C; Yahsi U. The effect of hole fraction on viscosity in atactic and syndiotactic polystyrenes. International Journal of Thermophysics. 2015;36(10-11):3239–54. https://doi.org/10.1007/s10765-015-1990-4
21. Sahin-Dinc F; Yahsi U; Sedlacek T. Interrelationships of pressure-dependent hole fraction and elongational viscosity in polymer melts. Advances in Polymer Technology. 2019. https://doi.org/10.1155/2019/9493769
22. Yahsi U; Ulutas K; Tav C; Deger D. On the ionic conductivity of polymer electrolytes in terms of hole fraction. Journal of Polymer Science Part B-Polymer Physics. 2008, 46(20):2249–54. https://doi.org/10.1002/polb.21556
23. Yahsi U; Coskun B; Yumak A; Boubaker K; Tav C. Relaxation time of polypropylene glycol and polypropylene glycol dimethylether-like polymers in terms of fluid-phase temperature and pressure dependent hole fraction. European Polymer Journal. 2015, 68:226–32. https://doi.org/10.1016/j.eurpolymj.2015.04.038
24. Kansy J. Microcomputer program for analysis of positron annihilation lifetime spectra. Nuclear Instruments and Methods in Physics Research Section A: Accelerators, Spectrometers, Detectors and Associated Equipment. 1996, 374(2):235–44. https://doi.org/10.1016/0168-9002(96)00075-7
25. Eldrup M; Lightbody D; Sherwood JN. The temperature dependence of positron lifetimes in solid pivalic acid. Chemical Physics. 1981, 63(1-2):51–8. https://doi.org/10.1016/0301-0104(81)80307-2
26. Tao SJ. Positronium annihilation in molecular substances. The Journal ofChemical Physics. 1972;56(11):5499–510. https://doi.org/10.1063/1.1677067
27. Yu Z; Yahsi U; McGervey JD; Jamieson AM; Simha R. Molecular weight-dependence of free volume in polystyrene studied by positron annihilation measurements. Journal of Polymer Science Part B: Polymer Physics. 1994, 32(16):2637–44. https://doi.org/10.1002/polb.1994.090321609
28. Erkmen ZE. The effect of heat treatment on the morphology of D-Gun sprayed hydroxyapatite coatings. Journal of Biomedical Materials Research. 1999;48(6):861–8. https://doi.org/10.1002/(sici)1097-4636(1999)48:6<861::Aid-jbm15>3.0.Co;2-h
29. Mahnicka-Goremikina L; Svinka R; Svinka V; Grase L; Goremikins V. The formation of phases with low or negative linear thermal expansion coefficient in porous mullite ceramics. Epitoanyag - Journal of Silicate Based and Composite Materials. 2020;72(3):91–8. 10.14382/epitoanyag-jsbcm.2020.15
30. Mangla O; Roy S. Monoclinic zirconium oxide nanostructures having tunable band gap synthesized under extremely non-equilibrium plasma conditions. Proceedings. 2019;3(1):10. https://doi.org/10.3390/IOCN_2018-1-05486
31. Ledesma-Carrión DE. Optimization of synthesis process of nano-hydroxyapatite. In Transactions on Engineering Technologies, 2016; pp 143–53.
32. Rendtorff N; Garrido L; Aglietti E. Mullite–zirconia–zircon composites: Properties and thermal shock resistance. Ceramics International. 2009;35(2):779–86. https://doi.org/10.1016/j.ceramint.2008.02.015
33. Rittidach T; Tithito T; Suntornsaratoon P; Charoenphandhu N; Thongbunchoo J; Krishnamra N, et al. Effect of zirconia-mullite incorporated biphasic calcium phosphate/biopolymer composite scaffolds for bone tissue engineering. Biomedical Physics & Engineering Express. 2020;6(5). https://doi.org/10.1088/2057-1976/aba1c2
34. Morsy R; Elsayed M; Krause-Rehberg R; Dlubek G; Elnimr T. Positron annihilation spectroscopic study of hydrothemally synthesized fine nanoporous hydroxyapatite agglomerates. J Eur Ceram Soc. 2010, 30(9):1897–901. https://doi.org/10.1016/j.jeurceramsoc.2010.03.014

How to cite this article: Akay LN, Kalkandelen C, Akti N, Sengul MS, Tav C, Yahsi U, et al. Effects of sintering and zirconmullite doping on nanostructural vacancies of bovine hydroxyapatite by positron techniques. J Am Ceram Soc. 2023;1–8. https://doi.org/10.1111/jace.18985